RESEARCH ARTICLE
SPACE PHYSICS

Earth and Planetary Physics
9: 1–9, 2025
doi: 10.26464/epp2025005

Extended pan-spectrum fitting of energetic particle spectra

WenYan Li, LingHua Wang*, YongFu Wang*, XinNian Guo, and QianYi Ma

School of Earth and Space Sciences, Peking University, Beijing 100871, China

Key Points:

- We construct an EPS formula to self-consistently determine the spectral shape of energetic particles over a wide energy range that often shows two spectral transitions/breaks.
- The EPS (extended pan-spectrum) formula incorporates previously proposed spectral forms, as well as their combined forms.
- This fitting helps us compare the spectral features of different energetic particles, including their evolutions.

Citation: Li, W. Y., Wang, L. H., Wang, Y. F., Guo, X. N., and Ma, Q. Y. (2025). Extended pan-spectrum fitting of energetic particle spectra. *Earth Planet. Phys.*, *9*(2), 1–9. http://doi.org/10.26464/epp2025005

Abstract: The energy spectrum of energetic particles in space often shows a non-thermal spectral shape with two spectral transitions/breaks over a wide energy range, carrying crucial information about their acceleration, release and transportation process. To self-consistently characterize the spectral features of energetic particles, here we propose a novel extended pan-spectrum (EPS) formula to fit the particle energy-flux spectrum, which has the merit that can incorporate many commonly used spectrum functions with one spectral transition, including the pan-spectrum, double-power-law, Kappa, Ellison-Ramaty (ER) functions, etc. The formula can also determine the spectral shape with two spectral transitions, including the triple-power-law function, Kappa distribution (at low energy) plus power law (at high energy), power law (at low energy) plus ER function, etc. Considering the uncertainties in both J and E, we can fit this EPS formula well to the representative energy spectra of various particle phenomena in space, including solar energetic particles (electrons, protons, ^{3}He and heavier ions), anomalous cosmic rays, solar wind suprathermal particles (halo and superhalo electrons; pick-up ions and the suprathermal tail), etc. Therefore, the EPS fitting can help us self-consistently determine the spectral features of different particle phenomena, and improve our understanding of the physical nature of the origin, acceleration, and transportation of energetic particles in space.

Keywords: energy spectrum fitting; solar energetic particle; solar wind suprathermal particle; anomalous cosmic ray; pick-up ion

1. Introduction

Energetic particles are commonly observed in space, including solar energetic particles (SEPs) (Ellison and Ramaty, 1985; Lin RP, 1985; Lin RP and Schwartz, 1987; Mason et al., 2002; Mewaldt et al., 2005; Wang LH et al., 2006, 2022; Krucker et al., 2009; Wang XD et al., 2022; Wei WW et al., 2022), solar wind suprathermal particles (Lin RP, 1998; Gloeckler, 2003; Mason and Gloeckler, 2012; Yoon et al., 2012; Wang LH et al., 2015, 2022; Tao JW et al., 2016, 2021), galactic cosmic rays (Cummings et al., 2016), anomalous cosmic rays (ACRs) (Senanayake et al., 2015), energetic particles in magnetosphere (Zong Q-G et al., 2017; Ye YG et al., 2021; Chen JL et al., 2024), etc. The space-borne and ground observations suggest that, in a wide energy range, these energy particle populations show a non-thermal spectrum of particle intensity versus energy, often with one or two spectral transitions/breaks (Lin RP and Schwartz, 1987; Krucker et al., 2009; Wang LH, 2022). For example, Lin RP (1985) reported that the SEP electrons exhibited a power-law flux energy spectrum bending upward at energies above ~10 keV, then turning downward at energies above ~100 keV. The observed energy spectral shape can reflect the physical nature of these energetic particles' origins, acceleration, and transportation processes.

It is customary to characterize the spectral features by fitting the observed particle energy spectrum to a parameterized formula. However, many previous studies obtained the spectral features by fitting the energetic particle observation to a function with an assumed spectral shape involving no more than one spectral transition. For instance, the SEP electrons (Wang LH et al., 2006; Krucker et al., 2009) were often fitted to a single-power-law (SPL) energy spectrum expressed as $J(E) = A \times E^{-\beta}$, or a classical double-power-law (DPL) spectrum expressed as

$$J(E) = \begin{cases} A \times \left(\frac{E}{E_0}\right)^{-\beta_1}, & E < E_0 \\ A \times \left(\frac{E}{E_0}\right)^{-\beta_2}, & E > E_0 \end{cases}, \quad (1)$$

where E is the particle energy, J is the particle intensity (flux or fluence), A is the amplitude, E_0 is the break energy, and β, β_1 or β_2 is the power-law spectral index. The SEP protons (Ellison and Ramaty, 1985; Mewaldt et al., 2005) were typically fitted to an Ellison–Ramaty (ER) spectrum as

$$J(E) = A \times E^{-\beta} \mathrm{e}^{-\frac{E}{E_c}},$$

where E_c is the cutoff energy. In addition, the SEP ^{3}He-rich ions

First author: W. Y. Li, 1642264501lwy@pku.edu.cn
Correspondence to: L. H. Wang, wanglhwang@gmail.com
Y. F. Wang, wyffrank@gmail.com
Received 10 APR 2024; Accepted 07 NOV 2024.
First Published online 30 DEC 2024.

often show a power-law or curved energy spectrum (Mason et al., 2002). On the other hand, the solar wind suprathermal electrons (Tao JW et al., 2016, 2021; Wang LH, 2022) consist of halo/strahl populations at ~0.1−2 keV that were generally fitted to a Kappa distribution, expressed as

$$J(E)=\frac{En_0}{\pi m_e^{1/2}(2\kappa W_0)^{3/2}}\frac{\Gamma(\kappa+1)}{\Gamma\left(\kappa-\frac{1}{2}\right)\Gamma\left(\frac{3}{2}\right)}\left(1+\frac{E}{\kappa W_0}\right)^{-(\kappa+1)}, \tag{2}$$

with the Kappa index κ, the number density n_0 and the efficient temperature W_0, as well as a superhalo population at energies above 2 keV that is fitted well to an SPL energy spectrum.

Recently, Liu ZX et al. (2020) constructed a pan-spectrum fitting formula with continuous energy derivatives of J at any orders, which incorporates a generalized DPL function, SPL function, ER function, Kappa function, Maxwellian function, logarithmic-parabola (LP) function, etc. Therefore, the pan-spectrum formula can be utilized for self-consistently determining the spectral shape of energetic/suprathermal particles with no more than one spectral transition/break, as well as characterizing the sharpness/width of a spectral transition. Furthermore, they improved the spectrum fitting method by considering the uncertainties in both particle intensity and energy.

In this paper, we further propose an extended pan-spectrum fitting formula with eight parameters, in order to self-consistently determine the spectral shape of energetic particles over a wide energy range with two spectral transitions/breaks. Moreover, we develop a fitting method that can help to comparatively investigate the spectral properties between various energetic particle phenomena.

2. Extended Pan-Spectrum (EPS) Formula

2.1 Construction of EPS Formula

To fit the single-break energy spectra, Liu ZX et al. (2020) proposed a pan-spectrum formula,

$$J(E)=A\times E^{-\beta_1}\left[1+\left(\frac{E}{E_0}\right)^{\alpha}\right]^{\frac{\beta_1-\beta_2}{\alpha}},$$

integrated from

$$\frac{\mathrm{d}\ln J}{\mathrm{d}\ln E}=-\frac{\beta_1+\beta_2}{2}+\frac{\beta_1-\beta_2}{2}\tanh\left(\frac{\alpha(\ln E-\ln E_0)}{2}\right),$$

with continuous derivatives at any orders. It's noted that the pan-spectrum formula was so named because it can incorporate many previously used spectrum formulae, typically with a single break energy, including classical DPL, ER, Kappa, Maxwellian function, etc., as special cases.

In order to achieve a full-range energy spectrum fitting for the common situations of one or two break energies, we extend the formalism of pan-spectrum to a formula named the "Extended pan-spectrum (EPS) Formula", that can fit a spectral shape with 0, 1, or 2 spectral transitions/breaks. The EPS formula simultaneously meets the following requirements: (1) it can be divided into three segments clearly; (2) it can merge the three segments into one or two parts. We utilize two smooth tanh functions at break energies:

$$\frac{\mathrm{d}\ln J}{\mathrm{d}\ln E}=-\frac{\beta_1+\beta_3}{2}+\frac{\beta_1-\beta_2}{2}\tanh\left(\frac{\alpha_1(\ln E-\ln E_1)}{2}\right)+\frac{\beta_2-\beta_3}{2}\tanh\left(\frac{\alpha_2(\ln E-\ln E_2)}{2}\right). \tag{3}$$

Based on the property that when $x\to-\infty(+\infty)$, $\tanh(x)\to-1(+1)$, it satisfies the piecewise requirement:

$$\frac{\mathrm{d}\ln J}{\mathrm{d}\ln E}=\begin{cases}-\beta_1, & E\ll E_1\\ -\beta_2, & E_1\ll E\ll E_2\\ -\beta_3, & E\gg E_2\end{cases}. \tag{4}$$

After integrating Equation (3) over the energy E, we obtain the formula of $J(E)$ as:

$$J(E)=A\times E^{-\beta_1}\left[1+\left(\frac{E}{E_1}\right)^{\alpha_1}\right]^{\frac{\beta_1-\beta_2}{\alpha_1}}\left[1+\left(\frac{E}{E_2}\right)^{\alpha_2}\right]^{\frac{\beta_2-\beta_3}{\alpha_2}}, \tag{5}$$

where A is the amplitude coefficient, α_1 and α_2 (>0) determines the sharpness and width of energy transitions centering at E_1 and E_2, β_1, β_2, and β_3, respectively indicate the spectral indexes of three segments. As defined by Liu ZX et al. (2020), the spectral transition/break becomes smoother with increased width as the parameter α (>0) decreases. Figure 1 compares the sharpness/width of spectral transition when $\alpha_1=2$ (top panels) and $\alpha_2=10$ (bottom panels). In addition, the all-order derivatives of the EPS formula are continuous, with the 1st-order derivative being the combination of tanh functions and the 2nd-order derivative containing 2 dips.

2.2 Different Limiting Approximations

2.2.1 Three segments

(1) Generalized triple-power-law (TPL)

The formula can be rewritten as a continuous function (Wang W et al., 2023):

$$J(E)\propto\begin{cases}E^{-\beta_1}\left[1+\left(\frac{E}{E_1}\right)^{\alpha_1}\right]^{\frac{\beta_1-\beta_2}{\alpha_1}}\left[1+\left(\frac{E}{E_2}\right)^{\alpha_2}\right]^{\frac{\beta_2-\beta_3}{\alpha_2}}, & E<E_1\mathrm{e}^{-\frac{2}{\alpha_1}}\\ E^{-\frac{\beta_1+\beta_2}{2}}\left[\left(\frac{E}{E_1}\right)^{\frac{\alpha_1}{2}}+\left(\frac{E}{E_1}\right)^{-\frac{\alpha_1}{2}}\right]^{\frac{\beta_1-\beta_2}{\alpha_1}}\left[1+\left(\frac{E}{E_2}\right)^{\alpha_2}\right]^{\frac{\beta_2-\beta_3}{\alpha_2}}, & E_1\mathrm{e}^{-\frac{2}{\alpha_1}}\le E\le E_1\mathrm{e}^{\frac{2}{\alpha_1}}\\ E^{-\beta_2}\left[1+\left(\frac{E}{E_1}\right)^{-\alpha_1}\right]^{\frac{\beta_1-\beta_2}{\alpha_1}}\left[1+\left(\frac{E}{E_2}\right)^{\alpha_2}\right]^{\frac{\beta_2-\beta_3}{\alpha_2}}, & E_1\mathrm{e}^{\frac{2}{\alpha_1}}<E<E_2\mathrm{e}^{-\frac{2}{\alpha_2}}\\ E^{-\frac{\beta_2+\beta_3}{2}}\left[1+\left(\frac{E}{E_1}\right)^{-\alpha_1}\right]^{\frac{\beta_1-\beta_2}{\alpha_1}}\left[\left(\frac{E}{E_2}\right)^{\frac{\alpha_2}{2}}+\left(\frac{E}{E_2}\right)^{-\frac{\alpha_2}{2}}\right]^{\frac{\beta_2-\beta_3}{\alpha_2}}, & E_2\mathrm{e}^{-\frac{2}{\alpha_2}}\le E\le E_2\mathrm{e}^{\frac{2}{\alpha_2}}\\ E^{-\beta_3}\left[1+\left(\frac{E}{E_1}\right)^{-\alpha_1}\right]^{\frac{\beta_1-\beta_2}{\alpha_1}}\left[1+\left(\frac{E}{E_2}\right)^{-\alpha_2}\right]^{\frac{\beta_2-\beta_3}{\alpha_2}}, & E>E_2\mathrm{e}^{\frac{2}{\alpha_2}}\end{cases} \tag{6}$$

where the three segments are connected by two smooth transitions (when α_1 and α_2 are finite). The transition energies here are defined as

$$\left[E_1\mathrm{e}^{-\frac{2}{\alpha_1}},E_1\mathrm{e}^{\frac{2}{\alpha_1}}\right]\text{ and }\left[E_2\mathrm{e}^{-\frac{2}{\alpha_2}},E_2\mathrm{e}^{\frac{2}{\alpha_2}}\right].$$

When both α_1 and α_2 approach infinity, the formula is equivalent to a strict triple-power-law (TPL), which is simply described as:

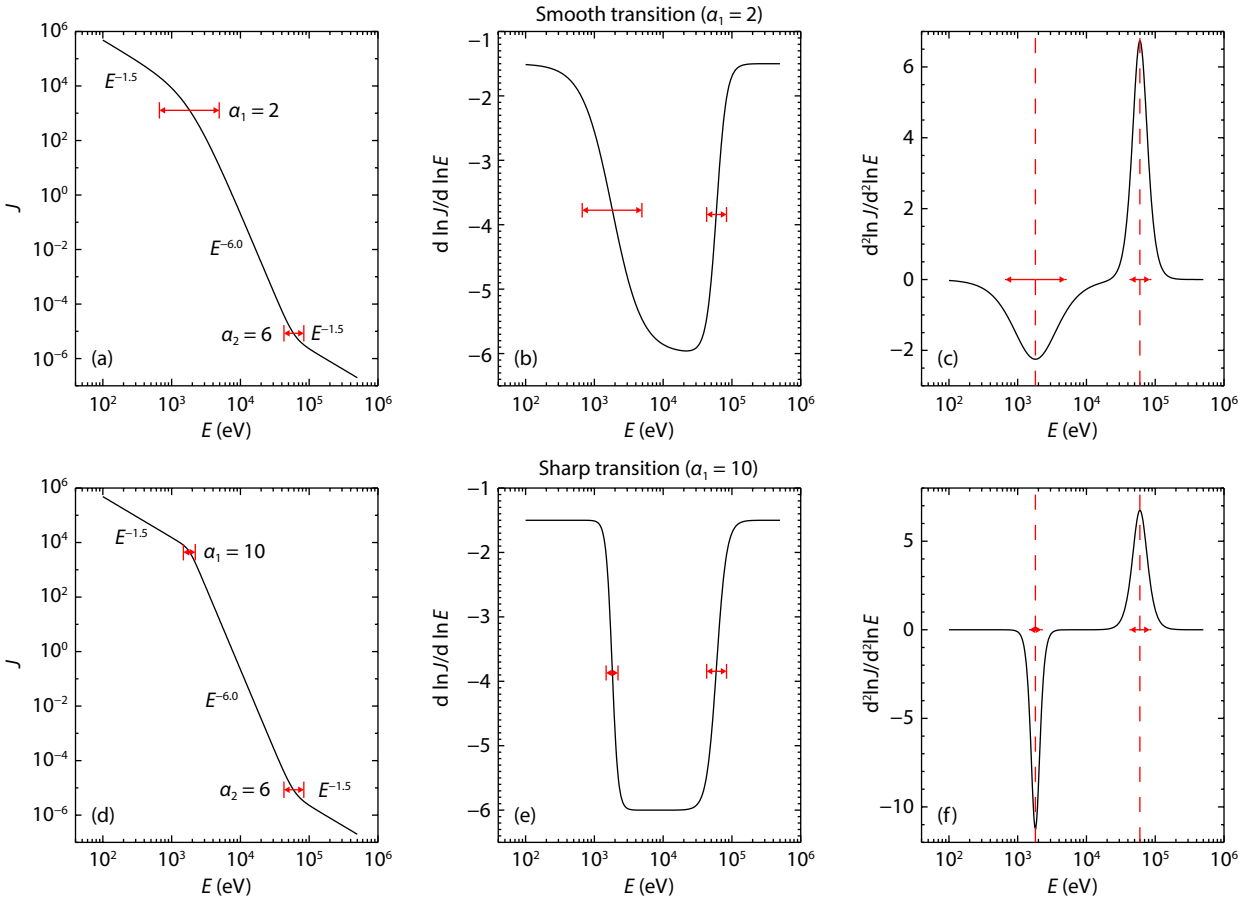

Figure 1. Curves of EPS formula (a, d), and its first-order (b, e) and second-order (c, f) derivative. The dashed lines indicate the central transition, and the double-ended arrows denote the transition widths. The top (bottom) panels show a smooth (sharp) transition with $\alpha_1 = 2$ ($\alpha_1 = 10$), when $\beta_1 = 1.5, \beta_2 = 6, \beta_3 = 1.5, E_1 = 1.8$ keV, and $E_2 = 60$ keV.

$$\lim_{\substack{\alpha_1\to\infty\\ \alpha_2\to\infty}} J(E) = \begin{cases} A\times\left(\dfrac{E}{E_1}\right)^{-\beta_1}, & \left(\dfrac{E}{E_1}\right)^{\alpha_1} \ll 1 \\ A\times\left(\dfrac{E}{E_1}\right)^{-\beta_2}, & \left(\dfrac{E}{E_2}\right)^{\alpha_2} \ll 1 \ll \left(\dfrac{E}{E_1}\right)^{\alpha_1} \\ A\times\left(\dfrac{E}{E_1}\right)^{-\beta_3}, & \left(\dfrac{E}{E_2}\right)^{\alpha_2} \gg 1. \end{cases} \tag{7}$$

(2) Kappa+SPL

When $\beta_1 = -1$ and $\alpha_1 = 1$, the formula is written as a continuous function:

$$\lim_{\substack{\beta_1=-1\\ \alpha_1=1}} J(E) \propto \begin{cases} E\left(1+\dfrac{E}{E_1}\right)^{-(\beta_2+1)}\left[1+\left(\dfrac{E}{E_2}\right)^{\alpha_2}\right]^{\frac{\beta_2-\beta_3}{\alpha_2}}, & \dfrac{E}{E_2} < \mathrm{e}^{-\frac{2}{\alpha_2}} \\ E^{1+\frac{\beta_2}{2}-\frac{\beta_3}{2}}\left(1+\dfrac{E}{E_1}\right)^{-(\beta_2+1)}\left[\left(\dfrac{E}{E_2}\right)^{\frac{\alpha_2}{2}}+\left(\dfrac{E}{E_2}\right)^{-\frac{\alpha_2}{2}}\right]^{\frac{\beta_2-\beta_3}{\alpha_2}}, & \mathrm{e}^{-\frac{2}{\alpha_2}} \le \dfrac{E}{E_2} < \mathrm{e}^{\frac{2}{\alpha_2}} \\ E^{-\beta_3}E^{(1+\beta_2)}\left(1+\dfrac{E}{E_1}\right)^{-(\beta_2+1)}\left[1+\left(\dfrac{E}{E_2}\right)^{\alpha_2}\right]^{\frac{\beta_2-\beta_3}{\alpha_2}}, & \dfrac{E}{E_2} > \mathrm{e}^{\frac{2}{\alpha_2}} \end{cases} \tag{8}$$

At low energies, $J(E)$ is a kappa-like distribution and the dominated part is $E\left(1+\dfrac{E}{E_1}\right)^{-(\beta_2+1)}$, where the kappa index κ is equivalent to β_2+1 and the efficient temperature is described as $W_0 = \dfrac{E_1}{\beta_2}$. The middle energies are in transition between Kappa-like distribution and power-law distribution, shown by the second part of function (8). At high energies, $J(E)$ is a power-law distribution, the spectral index of which is $-\beta_3$ times a distribution $E^{(1+\beta_2)}\left(1+\dfrac{E}{E_1}\right)^{-(\beta_2+1)}$, that tends to approach a constant when $E \gg E_1$. Therefore, when α_2 approaches infinity and $E_2 \gg E_1$, the limitation of the formula is:

$$\lim_{\substack{\beta_1=-1,\alpha_1=1\\ E_2\gg E_1}} J(E) \propto \begin{cases} E\left(1+\dfrac{E}{E_1}\right)^{-(\beta_2+1)}, & E \le E_2, \\ E^{-\beta_3}, & E > E_2. \end{cases} \tag{9}$$

(3) SPL+ER

When $\beta_3 \to \infty$ and $E_2 \to \infty$, the formula is written as a continuous function:

$$\lim_{\substack{\beta_3\to\infty\\ E_2\to\infty}} J(E) = A\times E^{-\beta_1}\left[1+\left(\frac{E}{E_1}\right)^{\alpha_1}\right]^{\frac{\beta_1-\beta_2}{\alpha_1}} \times \mathrm{e}^{-\left(\frac{E}{E_c}\right)^{\alpha_2}}, \quad E_c = E_2\left(\frac{\alpha_2}{\beta_3-\beta_2}\right)^{\frac{1}{\alpha_2}}, \tag{10}$$

where E_c, defined by E_2, α_2, β_2, and β_3, represents the cut-off energy that divides the ER function into a power-law below and

an exponential cut-off form above. This formula can be written in three parts, containing a power-law dominated part, a transition part, as well as an ER-dominated part:

$$\lim_{\substack{\beta_3\to\infty\\ E_2\to\infty}} J(E)\propto\begin{cases} E^{-\beta_1}\left[1+\left(\frac{E}{E_1}\right)^{\alpha_1}\right]^{\frac{\beta_1-\beta_2}{\alpha_1}}\times \mathrm{e}^{-\left(\frac{E}{E_c}\right)^{\alpha_2}}, & \\ & \frac{E}{E_1}<\mathrm{e}^{-\frac{2}{\alpha_1}} \\ E^{-\frac{\beta_2+\beta_3}{2}}\left[\left(\frac{E}{E_1}\right)^{\frac{\alpha_1}{2}}+\left(\frac{E}{E_1}\right)^{-\frac{\alpha_1}{2}}\right]^{\frac{\beta_1-\beta_2}{\alpha_1}}\times \mathrm{e}^{-\left(\frac{E}{E_c}\right)^{\alpha_2}}, & \\ & \mathrm{e}^{-\frac{2}{\alpha_1}}\le\frac{E}{E_1}<\mathrm{e}^{\frac{2}{\alpha_1}} \\ E^{-\beta_2}\mathrm{e}^{-\left(\frac{E}{E_c}\right)^{\alpha_2}}\left[1+\left(\frac{E}{E_1}\right)^{\alpha_1}\right]^{\frac{\beta_1-\beta_2}{\alpha_1}}, & \\ & \frac{E}{E_1}>\mathrm{e}^{\frac{2}{\alpha_1}} \end{cases} \tag{11}$$

when $E<E_1\ll E_c$, we can obtain $\mathrm{e}^{-\left(\frac{E}{E_c}\right)^{\alpha_2}}\to 1$, and when $\alpha_1\to\infty$, we can obtain the strict SPL + ER form:

$$\lim_{\substack{\beta_3\to\infty,E_2\to\infty\\ E_1\ll E_c}} J(E)\propto\begin{cases} E^{-\beta_1}, & E\ll E_1, \\ E^{-\beta_2}\mathrm{e}^{-\left(\frac{E}{E_c}\right)^{\alpha_2}}, & E\gg E_1. \end{cases} \tag{12}$$

(4) LP+LP

When $\alpha_2\to 0$, via Taylor expression of ln$J$, the formula is written as a continuous function:

$$\lim_{\alpha_2\to 0} J(E)=A\times E^{-\beta_1}\left[1+\left(\frac{E}{E_1}\right)^{\alpha_1}\right]^{\frac{\beta_1-\beta_2}{\alpha_1}} E^{\frac{\beta_2-\beta_3}{2}}\mathrm{e}^{\frac{\alpha_2(\beta_2-\beta_3)\ln^2 E}{8}}. \tag{13}$$

For simplicity, we use

$$\varphi(\alpha_i,E)=\frac{\alpha_i(\beta_i-\beta_{i+1})}{8}\ln^2 E,\ i=1,2$$

to refer to the quadratic term of Taylor expression. In Equation (13),

$$\mathrm{e}^{\frac{\alpha_2(\beta_2-\beta_3)\ln^2 E}{8}}$$

is rewritten as $\mathrm{e}^{\varphi(\alpha_2,E)}$, equivalent to $\ln J=\varphi(\alpha_2,E)$. Given that the logarithmic parabola term acts on the entire energy range $[0,+\infty]$, it should not be neglected when rewriting Equation (13) to three parts:

$$\lim_{\alpha_2\to 0} J(E)\propto\begin{cases} E^{-\beta_1}\left[1+\left(\frac{E}{E_1}\right)^{\alpha_1}\right]^{\frac{\beta_1-\beta_2}{\alpha_1}} E^{\frac{\beta_2-\beta_3}{2}}\mathrm{e}^{\varphi(\alpha_2,E)}, & \\ & \frac{E}{E_1}<\mathrm{e}^{-\frac{2}{\alpha_1}} \\ E^{-\frac{\beta_2+\beta_3}{2}}\left[\left(\frac{E}{E_1}\right)^{\frac{\alpha_1}{2}}+\left(\frac{E}{E_1}\right)^{-\frac{\alpha_1}{2}}\right]^{\frac{\beta_1-\beta_2}{\alpha_1}} E^{\frac{\beta_2-\beta_3}{2}}\mathrm{e}^{\varphi(\alpha_2,E)}, & \\ & \mathrm{e}^{-\frac{2}{\alpha_1}}\le\frac{E}{E_1}<\mathrm{e}^{\frac{2}{\alpha_1}} \\ E^{-\beta_2}\left[1+\left(\frac{E}{E_1}\right)^{-\alpha_1}\right]^{\frac{\beta_1-\beta_2}{\alpha_1}} E^{\frac{\beta_2-\beta_3}{2}}\mathrm{e}^{\varphi(\alpha_2,E)}. & \\ & \frac{E}{E_1}>\mathrm{e}^{\frac{2}{\alpha_1}} \end{cases} \tag{14}$$

When $\alpha_1\to\infty$, we can obtain a simplified form like:

$$\lim_{\substack{\alpha_1\to\infty\\ \alpha_2\to 0}} J(E)\propto\begin{cases} E^{-\beta_1+\frac{\beta_2-\beta_3}{2}}\mathrm{e}^{\varphi(\alpha_2,E)}, & E\ll E_1, \\ E^{-\frac{\beta_2+\beta_3}{2}}\mathrm{e}^{\varphi(\alpha_2,E)}, & E\gg E_1, \end{cases} \tag{15}$$

that is a combination of two logarithmic parabola at energies below or above E_1, accompanied with different energy axes of symmetry.

2.2.2 One or two segments

On one hand, when $\beta_2=\beta_3$, the formula degenerates to pan-spectrum form (Liu ZX et al., 2020),

$$J(E)=A\times E^{-\beta_1}\left[1+\left(\frac{E}{E_1}\right)^{\alpha_1}\right]^{\frac{\beta_1-\beta_2}{\alpha_1}},$$

which can fit well to a one- or two-segment spectrum. On the other hand, when $\beta_2\neq\beta_3$, the formula can also degenerate to fewer segments. For instance, when $\alpha_1\to 0$ and $\alpha_2\to 0$, the EPS formula is simplified to a logarithmic parabola:

$$\lim_{\substack{\alpha_1\to 0\\ \alpha_2\to 0}} J(E)\propto E^{-\frac{\beta_1+\beta_3}{2}}\mathrm{e}^{\varphi(\alpha_1,E)+\varphi(\alpha_2,E)} \tag{16}$$

or the form:

$$\lim_{\substack{\alpha_1\to 0\\ \alpha_2\to 0}} \ln J(E)=-\frac{\beta_1+\beta_3}{2}\ln E+\varphi(\alpha_1,E)+\varphi(\alpha_2,E)+\text{constant}, \tag{17}$$

with an infinite transition energy interval of $[0,+\infty]$. Note that the logarithmic parabola formula can't be characterized by fitting parameters themselves, and we usually use the slope at $E_{\min}$ and $E_{\max}$ or the energy axis of symmetry to depict the spectrum shape.

To summarize, the EPS formula can cover several formulae mentioned above (Equations (16)–(17)), under different limiting approximations, representing a powerful and versatile, generalized formula for interplanetary energetic spectra.

3. Methods

3.1 Fitting Method

Suggested by Liu ZX et al. (2020), we utilize the non-linear least-square algorithms to fit a series of n data points (x_i,y_i) to a parameterized function, $y=f(x,\boldsymbol{a})$, where $\boldsymbol{a}=(a_1,a_2,\ldots,a_m)$ is a vector of m undetermined parameters. By minimizing the reduced chi-square statistic (e.g., Bevington and Robinson, 2003; Liu ZX et al., 2020), the best fit is obtained.

In this study, for a serious of n data points (E_i,J_i), where E refers to the central energy of every energy channel and J refers to the flux at every energy channel, we fit the data points to our proposed EPS formula, $J=f(E,\boldsymbol{a})$, where $\boldsymbol{a}=(A_0,\beta_1,\beta_2,\beta_3,\ln E_1,\ln E_2,\alpha_1,\alpha_2)$ is an 8-dimensional vector. The reduced chi-square statistic is used to measure the error between the fitted and observed values. It is the sum of normalized residuals. Considering the uncertainties in both energies and fluxes suggested by Liu ZX et al. (2020), the reduced chi-square statistic is defined as,

$$\chi_\nu^2(\boldsymbol{a})=\frac{1}{n-m}\sum_{i=1}^{n}\frac{(J_i-f(E_i,a))^2}{\sigma_{J_i}^2+f_{E_i}'^2\sigma_{E_i}^2}, \tag{18}$$

where $\sigma_{E_i}^2$ ($\sigma_{J_i}^2$) is the standard deviation of observed E_i (J_i), m is the number of parameters, n is the number of data points, $n-m$ is the statistical degree of freedom, and $f_{E_i}^{'2} = \frac{\partial f}{\partial E}|_{E=E_i}$.

We utilize the Broyden-Fletcher-Goldfarb-Shanno (BFGS) algorithm (Broyden, 1970; Fletcher, 1987) to find the minimum of $\chi_\nu^2(\boldsymbol{a})$ in the multi-dimensional parameter space, which is an iterative method for solving unconstrained nonlinear optimization problems. The optimization problem is to minimize $\chi_\nu^2(\boldsymbol{a})$. It proceeds according to these steps:

Step (1) starts with a given initial estimate $\boldsymbol{a}^0$, a threshold ϵ where the iteration stops, and an iteration maximum number.

Step (2) calculates the gradient $\nabla f(\boldsymbol{a}_k)$. If $||\nabla f(\boldsymbol{a}_k)|| < \epsilon$, the iteration ends. Otherwise, the iteration moves on. (Note that $f(\boldsymbol{a}_k)$ here is the $\chi_\nu^2(\boldsymbol{a})$).

Step (3) obtains the searching direction by solving the quasi-Newton equation,

$$\boldsymbol{B}_k\boldsymbol{p}_k = -\nabla f(\boldsymbol{a}_k), \tag{19}$$

where $\boldsymbol{B}_k$ is an approximation of the Hessian matrix at $\boldsymbol{a}_k$, which is updated iteratively at each stage, and $\nabla f(\boldsymbol{a}_k)$ is the gradient of the function evaluated at $\boldsymbol{a}_k$.

Step (4) performs a one-dimensional optimization (line search) to find an acceptable step size α_k in the direction obtained in Step (3). $\alpha_k = \text{argmin}\, f(\boldsymbol{a}_k + \alpha\boldsymbol{p}_k)$, which means that α_k minimizes the equation $f(\boldsymbol{a}_k + \alpha\boldsymbol{p}_k)$.

Step (5) sets $\boldsymbol{s}_k = \alpha_k\boldsymbol{p}_k$ and updates $\boldsymbol{a}_{k+1} = \boldsymbol{a}_k + \boldsymbol{s}_k$.

Step (6) calculates

$$\boldsymbol{B}_{k+1} = \boldsymbol{B}_k + \frac{\boldsymbol{y}_k\boldsymbol{y}_k^{\mathrm{T}}}{\boldsymbol{y}_k^{\mathrm{T}}\boldsymbol{s}_k} - \frac{\boldsymbol{B}_k\boldsymbol{s}_k\boldsymbol{B}_k^{\mathrm{T}}\boldsymbol{s}_k^{\mathrm{T}}}{\boldsymbol{s}_k^{\mathrm{T}}\boldsymbol{B}_k\boldsymbol{s}_k}, \boldsymbol{y}_k = \nabla f(\boldsymbol{a}_{k+1}) - \nabla f(\boldsymbol{a}_k). \tag{20}$$

Step (7) takes $\boldsymbol{a}_{k+1} = \boldsymbol{a}_k$ and iteratively moves to Step (2).

Finally, the best fit $\boldsymbol{a}^{\text{fit}}$ is obtained. As for estimating the uncertainties of fitted parameters, as suggested by Liu ZX et al. (2020) and Press (2007), we derive the covariance matrix $\boldsymbol{C}$ of $\boldsymbol{a}$ from the Hessian matrix of

$$\chi^2 = (n-m)\chi_\nu^2, C = \left(\frac{\boldsymbol{H}}{2}\right)^{-1}$$

and

$$\boldsymbol{H}_{ij} = (n-m)\frac{\partial\chi_\nu^2}{\partial a_i \partial a_j}.$$

The fitted $\boldsymbol{a}^{\text{fit}}$ is the diagonal vector of matrix $\boldsymbol{C}$, and the standard deviation of fitted parameters is defined as

$$\delta\boldsymbol{a}_{fit}^i = \sqrt{\boldsymbol{C}_{ii}}.$$

Besides using χ_ν^2 to select the best results under a fitting model, in our fitting procedure, we also calculate

$$\text{ECVI} = \frac{n-m}{n-1}\chi_\nu^2 + \frac{2m}{n}$$

(Expected Cross-Validation Index) as a model selection index and a smaller ECVI indicates a better fit model (Liu ZX et al., 2020).

3.2 Parameter Analysis

We utilize parametric bootstrap (Efron, 1992; MacKenzie et al., 2017) to characterize the uncertainties of parameter estimation and test the correlations between parameters. Parametric bootstrap is based on the assumption that the initial data set is from a distribution of a specific parametric type. In this paper, the parametric model $J(E)$ is fitted by parameter vector $\boldsymbol{a}$, then bootstrapped random samples are drawn from this model based upon the initial data set. Repeating many times of fitting to the generated samples produces the probability distribution of fitted parameters.

In this study, given an initial parameter vector $\boldsymbol{a}$ = (e^{20}, 2.0, 1.0, 3.5, 1.1 keV, 13.4 keV, 5.0, 3.0), we construct a group of 40 initial data points (E_i, J_i). Then we generate 1000 groups of random data points by adding a relative Gaussian noise of 0.05 to each data point in both E_i and J_i. Finally, we fit these 1000 groups of data to obtain a distribution of minimal chi-square and all fitted parameters. During the bootstrap simulation, around 180 samples are not converged and they are excluded in the statistical results that follow.

Figure 2 is the bootstrap simulation results for EPS formula with all eight parameters effective, one of which is closest to the initial parameters, shown in panel (b). The simulated χ_ν^2 probability distribution agrees with the ideal reduced chi-square distribution for 32 degrees of freedom in panel (a) (shown as dashed lines). Figure 2 (c–j) plot the histograms of the fitted parameters, indicating that all the spectral parameters are reasonably distributed, and in accordance with the initial parameters (shown as dashed lines).

In addition, Figure 3 plots the scatter diagrams between fitted parameters, also indicating that the averaged parameters (shown as green horizontal and vertical solid lines) agree with the initial parameters (shown as purple stars). We note: (1) the strong positive correlation between A_0 and β_1 with a correlation coefficient $CC > 0.7$; (2) the moderate positive correlation between β_2 and $\ln E_2$ with $0.5 < CC < 0.7$; (3) the moderate negative correlation between $\ln E_1$ and $\ln E_2$ with $0.5 < -CC < 0.7$. These correlations are reasonable. For example, if A_0 increases, β_1 will also increase, leading to the formation of a steeper spectrum, thus reducing the residuals over the full energy range.

4. Applications of EPS Formula

We apply the fitting method to the energy spectra of various representative particle phenomena that achieve the best and most reliable fit, with reasonable parameters, acceptable uncertainty estimations, as well as randomly distributed residuals. As for the fitting uncertainties, since the measurements given by different instruments behave differently, here we use both $\sigma_{E_i} = 0.05E_i$ and $\sigma_{J_i} = 0.05J_i$ for consistency.

Figure 4 and Table 1 show the fitted results of several typical particle phenomena. In Figure 4a, solar energetic electrons (SEEs) (Lin RP, 1985) are fitted to a strict TPL with two sharp transitions, that can be interpreted as a power-law of $E^{-\beta_1}$ at very low energies, $E^{-\beta_2}$ at middle energies that are far enough from both E_1 and E_2, and $E^{-\beta_3}$ at very high energies. By comparison, in Figure 4c, the O^+ in an SEP event (Mewaldt et al., 2005) shows a generalized TPL, with two smooth transitions, that are 0.28–0.54 and 1.2–15.5 MeV/nuc. In Figure 4e, the halo and superhalo electrons (Yoon et

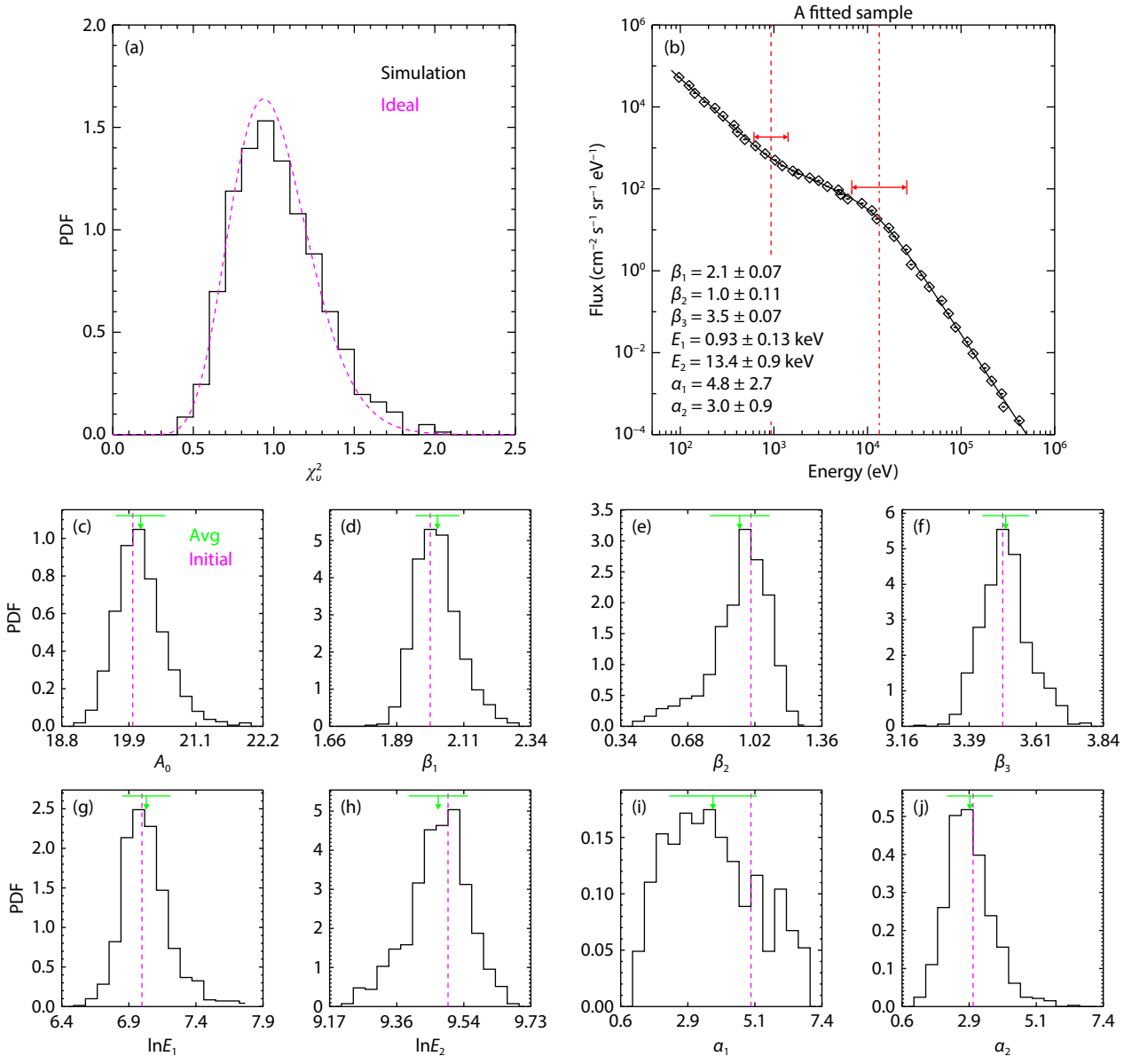

Figure 2. Histograms of fitted parameters and one fitted sample in bootstrap simulation. (a) The probability distribution function (PDF) of simulated minimal χ^2_υ for the 1000 test samples, compared with the ideal reduced chi-square distribution (dashed line). (b) A sample in the simulation, with fitted parameters written in, central transitions shown in red dashed lines, and transition widths shown in double-ended arrows. (c–j) The PDF of the eight simulated parameters, with the simulation initial parameters shown in dashed lines and the simulated average values with standard deviations shown in green arrows.

al., 2012) in quiet solar wind are fitted to the combination (red line) of a kappa distribution at low energies (shown in purple text), and an SPL tail at high energies (shown in blue text). The fitting is performed at suprathermal energies with a flux intensity at least five times higher than the thermal Maxwellian distribution estimate (Guo XN et al., 2024)**.** The close fit observed here validates our limit hypothesis. Furthermore, previous studies chose to fit the halo electrons and superhalo tail separately by dividing the energies (Yoon et al., 2012; Wang LH, 2022), with similar results to our monolithic fitting. In Figure 4g, the ions in a stream interaction region (SIR) event (Wei WW et al., 2022) seem to show a combined spectrum of SPL and ER-like tail at energies below/above 0.56 MeV/nuc. Figures 4i and k apply the method to other usual phenomena: the pick-up ions (PUI), the suprathermal tail (Gloeckler, 2003; Mason and Gloeckler, 2012), and the ACRs (Senanayake et al., 2015). Each are generally well-fitted to the EPS formula. Note that the EPS fitting method has already taken into account the effects of data from different instruments with different energy channel resolutions, by considering the energy bandwidth (energy error) of observations. In addition, the presence of data gaps could affect the uncertainty estimates (see Figure 4).

5. Conclusion

In this study, we construct an EPS formula (Equation (5)) to self-consistently determine the spectral shape of energetic particles over a wide energy range that often show two spectral transi-

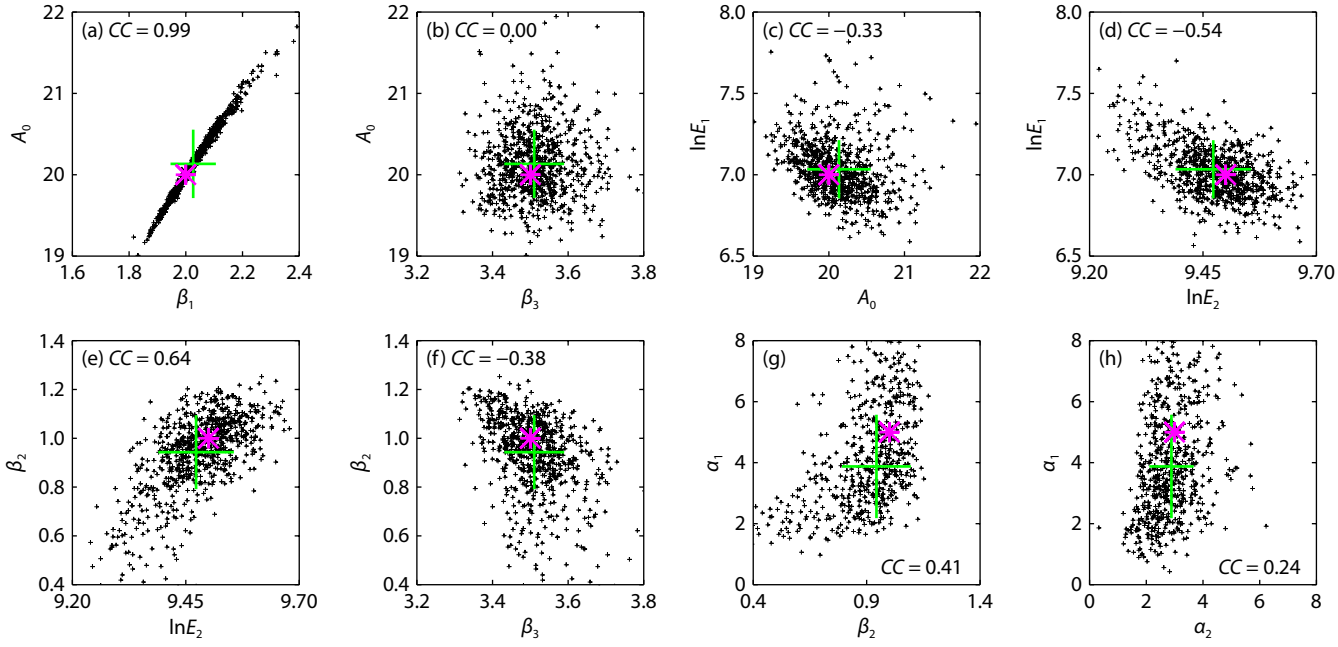

Figure 3. Scatter plots between parameters in bootstrap simulation. The purple stars denote the initial parameters, and the green horizontal and vertical solid lines denote the standard deviations of the simulated parameters.

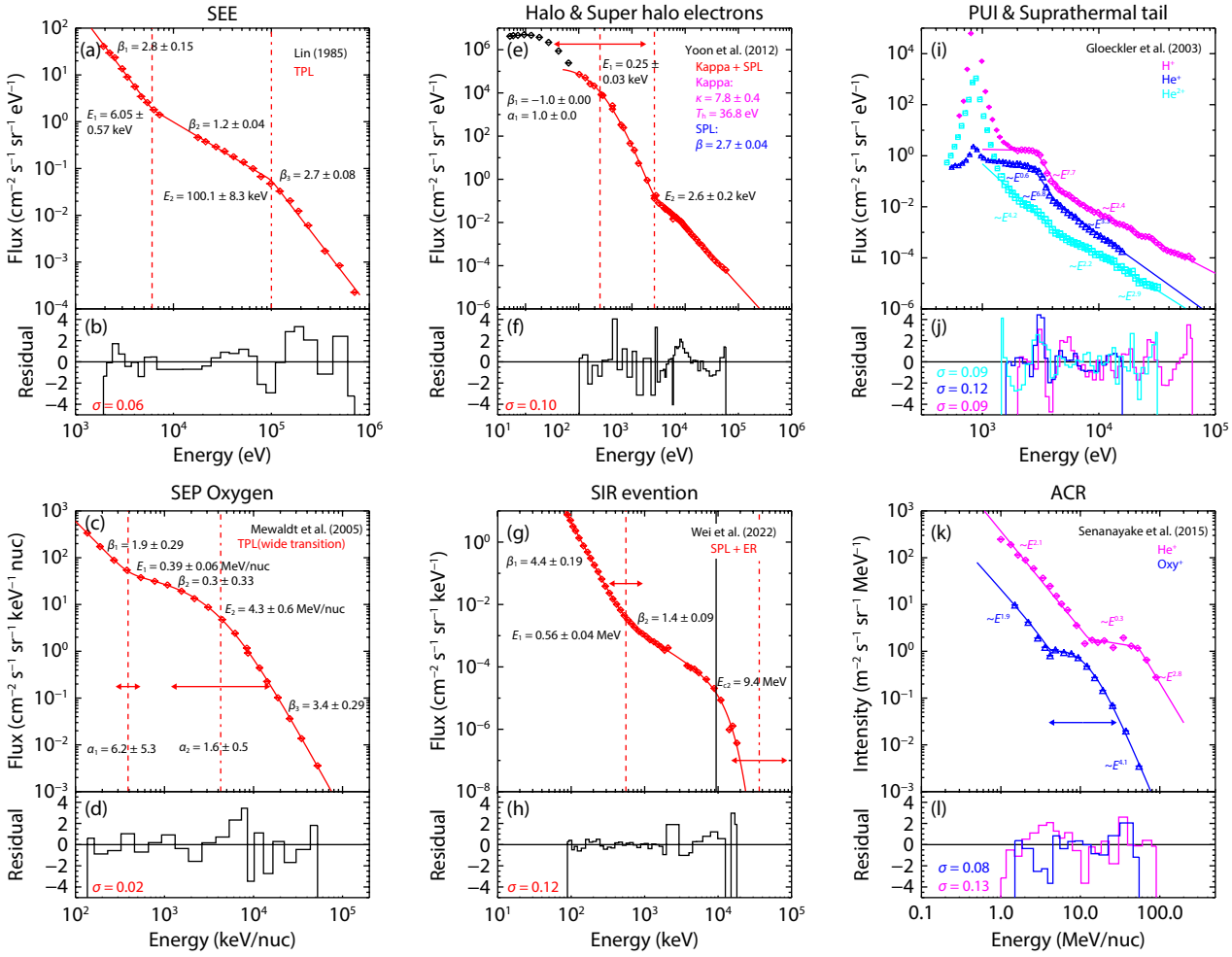

Figure 4. Best fits and the normalized residuals of the representative energy spectra of SEE (a–b), SEP O^+ (c–d), halo and super halo electrons in solar wind (e–f), SIR ions (g–h), pick-up ions and the suprathermal tail (i–j), and ACRs (k–l). The colored lines are explained by the text in each panel, either for different formula parts or for different ion species.

Table 1. Fitted parameters of Figure 4.

		β_1	β_2	β_3	E_1	E_2	α_1	α_2
SEE		2.8 ± 0.2	1.24 ± 0.04	2.72 ± 0.08	6.1 ± 0.6 keV	100 ± 8 keV	30[a]	25[a]
SEP O^+		1.9 ± 0.3	0.3 ± 0.3	3.4 ± 0.3	0.39 ± 0.06 MeV/nuc	4.3 ± 0.6 MeV/nuc	6.2 ± 5.3	1.2 ± 0.5
Halo & superhalo solar wind		−1[a]	6.8 ± 0.4	2.74 ± 0.04	0.25 ± 0.03 keV	2.6±0.2 keV	1[a]	10 ± 5.5
SIR ions		4.2 ± 0.2	1.43 ± 0.09	infinity	0.56 ± 0.04 MeV/nuc	infinity	3.8 ± 1.1	2.3 ± 0.1
PUI & suprathermal tail	H^+	0.1 ± 0.1	7.7 ± 0.4	2.37 ± 0.01	2.86 ± 0.04 keV	4.7 ± 0.1 keV/nuc	102[a]	57[a]
	He^+	0.59 ± 0.08	6.8 ± 0.4	3.27 ± 0.07	2.66 ± 0.03 keV	4.5 ± 0.3 keV/nuc	56[a]	70[a]
	He^{2+}	4.20 ± 0.07	2.24 ± 0.06	2.90 ± 0.07	4.7 ± 0.2 keV	12.3 ± 0.7 keV/nuc	89[a]	77[a]
ACR	He	2.08 ± 0.04	0.28 ± 0.05	2.8 ± 0.4	12.8 ± 0.4 keV/nuc	53 ± 3 keV/nuc	37[a]	27[a]
	O	1.9 ± 0.5	−0.9 ± 1.3	4.1 ± 0.7	4.2 ± 0.1 keV/nuc	11 ± 2 keV/nuc	20[a]	2.0 ± 1.0

Note: [a] Parameters with no uncertainties indicate the data points are fitted under limiting approximations.

tions/breaks. The EPS formula has eight parameters: the amplitude coefficient A; central energy E_1 and E_2 of low-energy and high-energy spectral transition; sharpness parameter α_1 and α_2 of low-energy and high-energy transition; and power-law spectral index β_1, β_3, and β_2, respectively, at energies below the low-energy transition, above the high-energy transition, and between the two transitions.

This EPS formula can be rewritten as a piecewise form of generalized TPL. When $\beta_2 = \beta_3$, it degenerates to the PS formula proposed by Liu ZX et al. (2020), which can self-consistently determine the spectral shape with one or no spectral transitions/breaks (e.g., the SPL, DPL, EP, Kappa, and LP functions). Furthermore, the EPS formula can be transformed under certain specific parameter conditions to spectral forms with two spectral transitions/breaks. For instance, a classical TPL with sharp spectral breaks when $\alpha_1\,(\alpha_2) \to \infty$, a Kappa distribution (at low energies) plus an SPL (at high energies) when $\beta_1 = -1, \alpha_1 = 1, \alpha_2 \to \infty$, and $E_1 \ll E_2$, an SPL (at low energies) plus an ER-like distribution (at high energies) when $E_2 \to \infty, \beta_3 \to \infty$, and $E_1 \ll E_c$, and an LP plus LP distribution when $\alpha_1 \to \infty$ and $\alpha_2 \to 0$.

Considering the uncertainties in both E and J, we utilize the BFGS algorithm (Broyden, 1970; Fletcher, 1987) in order to minimize $\chi^2_v(\boldsymbol{a})$ and achieve the best fit. The EPS formula fits well to the energy spectra of various energetic particle phenomena (Table 1 and Figure 4), including SEPs (electrons, protons, ^{3}He and heavier ions), solar wind suprathermal particles (halo and superhalo electrons; pick-up ions and the suprathermal tail), ACRs, etc. The EPS fitting method can self-consistently determine the spectral features of energetic particle phenomena without first assuming a given spectral shape. Therefore, it can help us comprehensively understand the origin, acceleration, and transport processes of energetic particles over a wide energy spectrum, as well as comparatively examine the physical properties of different energetic particle phenomena.

Acknowledgments

This research is supported in part by NSFC under contracts 42225404, 42127803, 42150105, by National Key R&D Program of China No. 2021YFA0718600, and by ISSI-BJ through the international teams Nos. 23-581 and 56. Code is available in a public repository (https://github.com/EpsilonLwy/EPS_fitting).

References

Bevington, P. R., and Robinson, D. K. (2003). *Data Reduction and Error Analysis for the Physical Sciences* (3rd ed, pp. 2383–2402). Boston: McGraw-Hill.

Broyden, C. G. (1970). The convergence of a class of double-rank minimization algorithms 1. General considerations. *IMA J. Appl. Math.*, *6*(1), 76–90. https://doi.org/10.1093/imamat/6.1.76

Chen, J. L., Zou, H., and Ye, Y. G. (2024). Explaining the dynamics of the sub-relativistic electron third belt in the Earth's radiation belts by using medium Earth orbit satellite observations. *Earth Planet. Phys.*, *8*(5), 762–775. https://doi.org/10.26464/epp2024054

Cummings, A. C., Stone, E. C., Heikkila, B. C., Lal, N., Webber, W. R., Jóhannesson, G., Moskalenko, I. V., Orlando, E., and Porter, T. A. (2016). Galactic cosmic rays in the local interstellar medium: *Voyager* 1 observations and model results. *Astrophys. J.*, *831*(1), 18. https://doi.org/10.3847/0004-637X/831/1/18

Efron, B. (1992). Bootstrap methods: another look at the jackknife. In: S. Kotz, et al. (Eds.), *Breakthroughs in Statistics: Methodology and Distribution* (pp. 569–593). New York: Springer. https://doi.org/10.1007/978-1-4612-4380-9_41

Ellison, D. C., and Ramaty, R. (1985). Shock acceleration of electrons and ions in solar flares. *Astrophys. J.*, *298*, 400–408. https://doi.org/10.1086/163623

Fletcher, R. (1987). *Practical Methods of Optimization* (2nd ed). Chichester: John Wiley & Sons. https://doi.org/10.1002/9781118723203

Gloeckler, G. (2003). Ubiquitous suprathermal tails on the solar wind and pickup ion distributions. *AIP Conf. Proc.*, *679*(1), 583–588. https://doi.org/10.1063/1.1618663

Guo, X. N., Wang, L. H., Li, W. Y., Ma, Q. Y., Yang, L., Wimmer-Schweingruber, R. F., and Bale, S. D. (2024). Evolution of electron acceleration by corotating interaction region shocks at 1 AU. *Astrophys. J.*, *966*(1), L12. https://doi.org/10.3847/2041-8213/ad3d5f

Krucker, S., Oakley, P. H., and Lin, R. P. (2009). Spectra of solar impulsive electron events observed near Earth. *Astrophys. J.*, *691*(1), 806–810. https://doi.org/10.1088/0004-637X/691/1/806

Lin, R. P. (1985). Energetic solar electrons in the interplanetary medium. *Sol. Phys.*, *100*(1-2), 537–561. https://doi.org/10.1007/BF00158444

Lin, R. P., and Schwartz, R. A. (1987). High spectral resolution measurements of a solar flare hard X-ray burst. *Astrophys. J.*, *312*, 462. https://doi.org/10.1086/164891

Lin, R. P. (1998). WIND observations of suprathermal electrons in the interplanetary medium. *Space Sci. Rev.*, *82*(1-2), 61–78. https://doi.org/10.1023/A:1005048428480

Liu, Z. X., Wang, L. H., Wimmer-Schweingruber, R. F., Krucker, S., and Mason, G.

M. (2020). Pan-spectrum fitting formula for suprathermal particles. *J. Geophys. Res.: Space Phys.*, *125*(12), e2020JA028702. https://doi.org/10.1029/2020JA028702

MacKenzie, D. I., Nichols, J. D., Royle, J. A., Pollock, K. H., Bailey, L., and Hines, J. E. (2017). *Occupancy Estimation and Modeling: Inferring Patterns and Dynamics of Species Occurrence* (pp. 115–215). Amsterdam: Elsevier. https://doi.org/10.1016/C2012-0-01164-7

Mason, G. M., Wiedenbeck, M. E., Miller, J. A., Mazur, J. E., Christian, E. R., Cohen, C. M. S., Cummings, A. C., Dwyer, J. R., Gold, R. E., … Von Rosenvinge, T. T. (2002). Spectral properties of He and heavy ions in ^{3}He-rich solar flares. *Astrophys. J.*, *574*(2), 1039–1058. https://doi.org/10.1086/341112

Mason, G. M., and Gloeckler, G. (2012). Power law distributions of suprathermal ions in the quiet solar wind. *Space Sci. Rev.*, *172*(1-4), 241–251. https://doi.org/10.1007/s11214-010-9741-0

Mewaldt, R. A., Cohen, C. M. S., Labrador, A. W., Leske, R. A., Mason, G. M., Desai, M. I., Looper, M. D., Mazur, J. E., Selesnick, R. S., and Haggerty, D. K. (2005). Proton, helium, and electron spectra during the large solar particle events of October–November 2003. *J. Geophys. Res.: Space Phys.*, *110*(A9), A09S18. https://doi.org/10.1029/2005JA011038

Press, W. H., Teukolsky, S. A., Vetterling, W. T., and Flannery, B. P. (2007). *Numerical Recipes: The art of Scientific Computing* (3rd ed). Cambridge: Cambridge University Press.

Senanayake, U. K., Florinski, V., Cummings, A. C., and Stone, E. C. (2015). Spectral evolution of anomalous cosmic rays at *voyager* 1 beyond the termination shock. *Astrophys. J.*, *804*(1), 12. https://doi.org/10.1088/0004-637X/804/1/12

Tao, J. W., Wang, L. H., Zong, Q. G., Li, G., Salem, C. S., Wimmer-Schweingruber, R. F., He, J. S., Tu, C. Y., and Bale, S. D. (2016). Quiet-time suprathermal (~0.1–1.5 keV) electrons in the solar wind. *Astrophys. J.*, *820*(1), 22. https://doi.org/10.3847/0004-637X/820/1/22

Tao, J. W., Wang, L. H., Li, G., Wimmer-Schweingruber, R. F., Salem, C., Jian, L. K., and Bale, S. D. (2021). Solar wind ~0.15–1.5 keV electrons around corotating interaction regions at 1 AU. *Astrophys. J.*, *922*(2), 198. https://doi.org/10.3847/1538-4357/ac2505

Wang, L. H., Lin, R. P., Krucker, S., and Gosling, J. T. (2006). Evidence for double injections in scatter-free solar impulsive electron events. *Geophys. Res. Lett.*, *33*(3), L03106. https://doi.org/10.1029/2005GL024434

Wang, L. H., Yang. L., He, J. S., Tu, C. Y., Pei, Z. T., Wimmer-Schweingruber, R. F., and Bale, S. D. (2015). Solar wind ~20–200 keV superhalo electrons at quiet times. *Astrophys. J. Lett.*, *803*(1), L2. https://doi.org/10.1088/2041-8205/803/1/L2

Wang, L. H. (2022). Interplanetary energetic electrons observed in Earth's polar cusp/cap/lobes. *Rev. Mod. Plasma Phys.*, *6*, 12. https://doi.org/10.1007/s41614-022-00073-5

Wang, W., Wang, L. H., Krucker, S., and Wimmer-Schweingruber, R. F. (2023). Energy spectrum of solar energetic electron events over 25 years. *Astrophys. J.*, *948*(1), 51. https://doi.org/10.3847/1538-4357/acbea2

Wei, W. W., Zhuang, B., Huang, J., Shen, F., Zhao, L. L., Liu, M. Z., Zhang, X. X., and Feng, X. S. (2022). Energy spectra variations of energetic ions associated with a stream interaction region. *J. Geophys. Res.: Space Phys.*, *127*(10), e2022JA030652. https://doi.org/10.1029/2022JA030652

Wang, X. D., Klecker, B., Nicolaou, G., Barabash, S., Wieser, M., Wurz, P., Galli, A., Cipriani, F., and Futaana, Y. (2022). Neutralized solar energetic particles for SEP forecasting: Feasibility study of an innovative technique for space weather applications. *Earth Planet. Phys.*, *6*(1), 42–51. https://doi.org/10.26464/epp2022003

Ye, Y. G., Zou, H., Zong, Q.-G., Chen, H. F., Zou, J. Q., Shi, W. H., Yu, X. Q., Zhong, W. Y., Wang, Y. F., ... Hao, X. Y. (2021). Energetic electron detection packages on board Chinese navigation satellites in MEO. *Earth Planet. Phys.*, *5*(2), 158–179. https://doi.org/10.26464/epp2021021

Yoon, P. H., Ziebell, L. F., Gaelzer, R., Lin, R. P., and Wang, L. (2012). Langmuir turbulence and suprathermal electrons. *Space Science Reviews*, *173*, 459–489. https://doi.org/10.1007/s11214-012-9867-3

Zong, Q.-G., Wang, Y. F., Ren, J., Zhou, X. Z., Fu, S. Y., Rankin, R., Zhang, H. (2017). Corotating drift-bounce resonance of plasmaspheric electron with poloidal ULF waves. *Earth Planet. Phys.*,, *1*(1), 2–12. https://doi.org/10.26464/epp2017002